

A comprehensive range of X-ray ionized-reflection models

R. R. Ross^{1★} and A. C. Fabian²

¹*Physics Department, College of the Holy Cross, Worcester, MA 01610, USA*

²*Institute of Astronomy, Madingley Road, Cambridge CB3 0HA*

Accepted 2005 January 2. Received 2004 December 22; in original form 2004 July 23

ABSTRACT

X-ray ionized reflection occurs when a surface is irradiated with X-rays so intense that its ionization state is determined by the ionization parameter $\xi \propto F/n$, where F is the incident flux and n the gas density. It occurs in accretion, on to compact objects including black holes in both active galaxies and stellar-mass binaries, and possibly in gamma-ray bursts. Computation of model reflection spectra is often time consuming. Here we present the results from a comprehensive grid of models computed with our code, which has now been extended to include what we consider to be all energetically important ionization states and transitions. This grid is being made available as an ionized-reflection model, REFLION, for XSPEC.

Key words: accretion, accretion discs – line: formation – radiative transfer – galaxies: active – X-rays: general.

1 INTRODUCTION

The process of backscattering and fluorescence of X-rays from cosmic matter known as X-ray reflection is commonly observed throughout astronomy. We are concerned here with the situation where the X-ray irradiation is so intense that it determines the ionization state of the material. This occurs in accreting X-ray sources such as Galactic black hole candidates (BHCs) and active Galactic nuclei (AGN), and may also be relevant to gamma-ray bursts (GRBs).

The irradiated gas is Compton thick, which requires that Comptonization of the radiation as well as the necessary atomic physics be dealt with. The results of such computations have been published over the last ten years, first for constant-density atmospheres (Ross & Fabian 1993; Życki et al. 1994; Ross, Fabian & Young 1999) and more recently for density structures in hydrostatic equilibrium (Nayakshin, Kazanas & Kallman 2000; Ballantyne, Ross & Fabian 2001; Różańska et al. 2002; Mauche et al. 2004). Reasonable agreement is found between most of these results (Péquignot et al. 2002).

Most methods are computationally very time consuming, so only limited regions of parameter space have been explored. Our method runs relatively rapidly, on the other hand, when the illuminated gas is assumed to have constant density. Such models are still useful for several reasons. The overall geometry is still not understood for many sources. Even when a simple accretion-disc structure is assumed, detailed calculations of hydrostatic equilibrium are subject to uncertainties in the total thickness of the disc (and hence the vertical component of the local gravitational field), the boundary condition (either pressure or height) at the base of the illuminated

layer, the external pressure exerted by the corona, the geometry of the illumination, the influence of magnetic fields, etc. Furthermore, Ballantyne et al. (2001) found that models for reflection by atmospheres in hydrostatic equilibrium could be fitted by diluted versions of constant-density reflection models.

We have now assembled an extended grid of models for which the ionization parameter, irradiating spectral index and iron abundance are free parameters. At the same time the original code has been expanded to include further ionization species. All abundant species and their important transitions are now included. The purpose of this paper is to present example spectra from across this grid which can be used as a guide to the interpretation of AGN, BHC and GRB X-ray spectra.

2 METHODS

2.1 Radiative transfer

Our calculations extend and improve on the models discussed by Ross et al. (1999). Now the illuminating radiation is assumed to have a cut-off power-law spectrum,

$$F_E = AE^{-\Gamma+1} \exp(-E/E_c), \quad (1)$$

that extends to higher photon energies. Different values of the photon index Γ are treated, while the cut-off energy is fixed at $E_c = 300$ keV. The amplitude A is chosen so that the total illuminating flux, $F_{\text{tot}} = \int F_E dE$, corresponds to a desired value of the ionization parameter,

$$\xi = \frac{4\pi F_{\text{tot}}}{n_H}. \quad (2)$$

The illumination is incident on the upper surface of a plane-parallel slab representing the top layer of an optically thick medium

★E-mail: rross@holycross.edu

such as an accretion disc. The slab has hydrogen number density $n_{\text{H}} = 10^{15} \text{ cm}^{-3}$ and Thomson depth $\tau_{\text{T}} \geq 5$. (Larger Thomson depths are treated for larger values of ξ , as the illumination can penetrate to greater depths when the gas is more highly ionized.) No net flux is allowed to enter the slab from below, so that the emergent radiation is owing entirely to reprocessed illumination ('reflection'). Additional radiation from beneath the surface layer could be approximated by adding a soft blackbody spectrum to the calculated reflection spectrum (see Section 4).

As described by Ross & Fabian (1993), the penetration of the illuminating radiation is treated separately from the transfer of the diffuse radiation produced via scattering or emission within the gas. In order to extend the treatment of the diffuse radiation to photon energies above 100 keV, Compton scattering is treated using the Fokker–Planck equation of Cooper (1971)

$$\left(\frac{\partial n}{\partial t} \right)_{\text{FP}} = \frac{n_{\text{e}} \sigma_{\text{T}}}{m_{\text{e}} c} \frac{1}{E^2} \frac{\partial}{\partial E} \left[\alpha(E, \theta) E^4 \left(n + \theta \frac{\partial n}{\partial E} \right) \right], \quad (3)$$

where n is the photon occupation number, E is the photon energy, n_{e} is the free-electron number density and $\theta = kT$. Here the Fokker–Planck equation of Kompaneets (1957) has been modified by the term

$$\alpha(E, \theta) = \frac{1 + \beta(\theta)/(1 + 0.02E)}{1 + 9 \times 10^{-3} E + 4.2 \times 10^{-6} E^2}, \quad (4)$$

with E in keV and with

$$\beta(\theta) = \frac{5}{2} \frac{\theta}{m_{\text{e}} c^2} + \frac{15}{8} \left(\frac{\theta}{m_{\text{e}} c^2} \right)^2 \left(1 - \frac{\theta}{m_{\text{e}} c^2} \right). \quad (5)$$

Equation (3) is applicable for $E \lesssim 1 \text{ MeV}$. The diffuse radiation field is taken to satisfy the steady-state Fokker–Planck/diffusion equation,

$$\left(\frac{\partial n}{\partial t} \right)_{\text{FP}} + \frac{\partial}{\partial z} \left(\frac{c}{3\kappa} \frac{\partial n}{\partial z} \right) + \frac{j_{\text{E}} h^3 c^3}{8\pi E^3} - c\kappa_{\text{A}} n \equiv 0, \quad (6)$$

where z is the vertical height within the slab, j_{E} is the spectral emissivity, $\kappa = \kappa_{\text{A}} + \kappa_{\text{KN}}$ is the total opacity (per volume), κ_{A} is the absorption opacity and κ_{KN} is the Klein–Nishina opacity for Compton scattering. We apply equation (6) to radiation with $10^{-3} < E < 10^3 \text{ keV}$. The energy resolution is $E/\Delta E = 50$ throughout the 0.1–10 keV spectral range (except for a resolution of 70 around the Fe $K\alpha$ lines), with somewhat lower resolution outside that range.

2.2 Atomic data

As the radiation field is relaxed to a steady state, the local temperature and fractional ionization of the gas are found by solving the equations of thermal and ionization equilibrium, as described by Ross & Fabian (1993). For this non-local thermodynamic equilibrium (non-LTE) calculation, we have extended the number of elements and the range of ions treated, and we have updated much of the atomic data employed. In addition to fully ionized species, the following ions are included in the calculations: C III–VI, N III–VII, O III–VIII, Ne III–X, Mg III–XII, Si IV–XIV, S IV–XVI and Fe IV–XXVI.

Photoionization cross sections for all subshells of the ions treated are calculated from the fits of Verner & Yakovlev (1995). Rates for direct collisional ionization and excitation autoionization are taken from Arnaud & Rothenflug (1985) and Arnaud & Raymond (1992). For carbon through sulphur, Auger ionization is treated as described by Weisheit & Dalgarno (1972). For iron, we employ the probabilities for multiple Auger ionization calculated by Kaastra & Mewe (1993), and a generalization of the method of Weisheit (1974) is used to calculate the resulting effect on the ionization balance.

For all elements except iron, total recombination rates as functions of density and temperature are derived from the tables of Summers (1974). These rates include two effects that are important at high densities: the increase in the recombination rate at low temperatures owing to three-body recombination and the reduction in the dielectronic recombination rate at high temperatures owing to collisional ionization of the highly excited states that follow radiationless recombination (Burgess & Summers 1969). At low densities, these rates are in reasonable agreement with more modern fits for combined radiative and dielectronic recombination (Arnaud & Rothenflug 1985). For iron, rates for radiative and dielectronic recombination are calculated using the fits of Arnaud & Rothenflug (1985) and Verner & Ferland (1996). Three-body recombination of iron is neglected, as it is unimportant at the densities under consideration (Jacobs et al. 1977). Rates for radiative recombination directly to ground levels are calculated using the Milne relation (e.g. Bates & Dalgarno 1962).

The most important emission lines for each ion are treated in the calculations. As the illuminated atmosphere is thick and dense, resonance lines are assumed to be optically thick ('case B'), greatly reducing the number of important lines. A total of 274 multiplets are included; individual lines within a multiplet are not resolved. Line energies and oscillator strengths for resonance lines are taken from the results of the Opacity Project (Verner, Verner & Ferland 1996). Excitation and line energies of nonresonance lines, as well as collision strengths for all lines, are derived from the CHIANTI data base (Dere et al. 2001). Parameter values missing from these data bases are taken from Kato (1976), Raymond & Smith (1977), Gaetz & Salpeter (1983), or Landini & Monsignor Fossi (1990) as necessary. The Fe $K\alpha$ lines treated are the recombination lines of Fe XXVI and Fe XXV (near 7.0 and 6.7 keV, respectively) and the fluorescence lines of Fe VI–XVI (near 6.4 keV). $K\alpha$ fluorescence of Fe XVII–XXII is assumed to be suppressed by autoionization (Auger effect) during resonance trapping (Ross, Fabian & Brandt 1996). Recombinations to excited levels of Fe XVII–XXII are assumed to result ultimately in $3s \rightarrow 2p$ line emission (Liedahl et al. 1990).

Resonance lines require special attention. Resonance-line photons can avoid destruction during resonance trapping by two mechanisms: Compton scattering out of the narrow line core between resonance scatterings and re-emission in the far line wings during resonance scattering. The fraction avoiding destruction is taken to be

$$f = \frac{(\kappa_{\text{T}}/\kappa)P_{\text{cont}} + P_{\text{esc}}}{P_{\text{cont}} + P_{\text{coll}} + P_{\text{esc}}}. \quad (7)$$

Here κ_{T} is the Thomson opacity, κ is the total continuum opacity at the line energy, P_{cont} is the probability per resonance scattering that the photon undergoes a continuum process (absorption or Compton scattering), and P_{coll} is the probability per resonance scattering that collisional de-excitation occurs instead of re-emission (Hummer 1968). The escape probability P_{esc} owing to re-emission in the far line wings (Hummer & Rybicki 1971) is calculated using the approximation for the K_2 function given by Hollenbach & McKee (1979). A Doppler line profile is assumed for all resonance lines except the Fe $K\alpha$ line, where a Lorentz profile is assumed owing to the importance of the damping wings. Line photons that avoid destruction during resonance trapping are added to the continuum by means of the local emissivity.

Elements lighter than iron are assumed to have solar abundances (Morrison & McCammon 1983), while the abundance of iron is set to a factor A_{Fe} times its solar value. Models are generated with underabundances as well as overabundances of iron. On the one

hand the X-ray spectra of some Seyfert galaxies appear to require high abundance of iron, for example MCG–6–30–15 (Fabian et al. 2002) and 1H 0707–49 (Boller et al. 2002), and Shemmer et al. (2004) have reported a strong correlation between metallicity and accretion rate in a sample of luminous quasars. On the other hand, Nomoto et al. (1997) have found that Type II supernovae produce the following average abundances relative to solar values: $A_C = 0.2$, $A_N = 0.01$, $A_O = 1.3$, $A_{Ne} = 0.9$, $A_{Mg} = 1.2$, $A_{Si} = 1.1$, $A_S = 0.7$ and $A_{Fe} = 0.35$. In that case, oxygen, neon, magnesium and silicon are near solar abundances, while the abundance of iron is markedly reduced.

2.3 Test case: an isolated slab

Recently Dumont et al. (2003) have criticized calculations, such as ours and those of Nayakshin et al. (2000), that employ the escape probability in treating emission lines. Dumont et al. use an ‘accelerated lambda iteration’ method that includes a detailed treatment of radiative transfer within the spectral lines themselves. They point out that their code has the drawback of being time-consuming, which precludes it from easily generating large grids of models for fitting data. In particular, they have applied their method to an *isolated* slab that is illuminated on one side. The total Thomson depth of the slab is $\tau_T = 4$, and the illuminating flux corresponds to $\xi = 10^3 \text{ erg cm s}^{-1}$. As a test of our method, we have performed our own computation for this situation. We cannot expect complete agreement because our calculations assume that helium is always fully ionized. Normally our interest is in reflection by a highly optically thick medium. In order for all of the incident energy to escape back out of the illuminated surface, the total radiative energy density increases with Thomson depth to such a degree that the assumption that helium is fully ionized should be satisfactory. When radiation is free to leave the far surface of a marginally thick slab, however, helium need not be fully ionized throughout. Dumont et al. (2003) found a large fraction of He^+ ions at depths $\tau_T \geq 3$. Our calculation of the isolated slab serves mainly as a test for the Lyman α ($\text{Ly}\alpha$) lines of H-like ions, which are produced in the hotter layers nearer the illuminated surface.

The biggest change required for this model is in the boundary condition at the far side of the slab. Diffuse radiation is allowed to emerge there, with the escaping flux calculated in the same way as at the illuminated surface (see Foster, Ross & Fabian 1986). Other changes must also be made to the method described previously. The gas density is reduced to $n_H = 10^{12} \text{ cm}^{-3}$. The illuminating spectrum is a simple power law with photon index $\Gamma = 2$ extending from 0.1 eV to 100 keV, and the energy resolution is fixed at $E/\Delta E = 30$. The metal abundances are set to the values of Allen (1973), which differ slightly from those of Morrison & McCammon (1983).

Fig. 1 shows the temperature structure and the ion fractions for oxygen and silicon that we calculate for the isolated slab. For $\tau_T \lesssim 2.5$, our results are in good agreement with those of Dumont et al. (2003). The differences at greater Thomson depth are presumably owing to the lack of He^+ in our model.

The reflected spectrum that we calculate for the isolated slab is shown in Fig. 2. Dumont et al. (2003) concluded that use of the escape probability must result in a drastic overestimation of the strength of the $\text{Ly}\alpha$ lines of H-like ions. However, we find the $\text{Ly}\alpha$ lines of C VI (0.37 keV), O VIII (0.65 keV), Mg XII (1.5 keV), Si XIV (2.0 keV) and S XVI (2.6 keV) to be in excellent agreement with their results. In particular, the O VIII line has an equivalent width of 27 eV with respect to the total (incident plus reflected) continuum, compared to their value of 28 eV. For the Si XIV

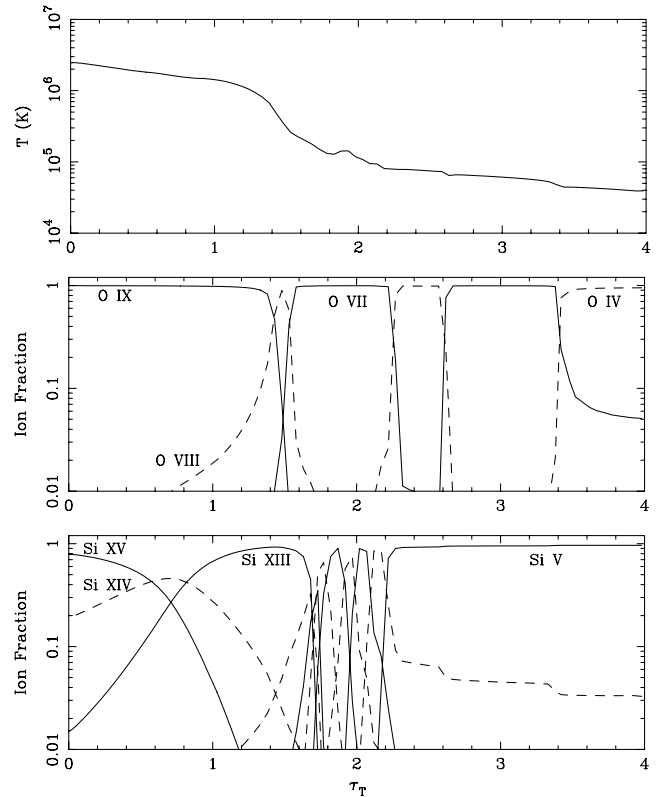


Figure 1. Structure as a function of Thomson depth for the *isolated* slab illuminated on one side. The upper panel shows the temperature, while the middle and bottom panels show the ion fractions of oxygen and silicon, respectively.

line, which is complicated by a steeper underlying continuum and blending with the He-like line, we estimate an equivalent width of 14 eV compared to their value of 9.5 eV. In our calculations, Compton scattering of resonance-line photons out of the narrow line core turns out to be much more important than re-emission in the far line wings. That is, the first term of the numerator in equation (7) completely dominates over the second term.

The Fe K α line is somewhat stronger in our calculation. As it is dominated by the Fe xxv intercombination line (6.7 keV), however, this is probably owing to different approximations in treating the atomic physics. Curiously, we find the $\text{Ly}\alpha$ line of N VII (0.50 keV) to be weaker than found by Dumont et al. (2003). Differences can be seen in other emission lines, but these are produced deeper within the slab, where He^+ could be a factor. Fig. 2 also shows the calculated spectrum emerging from the far side of the slab. Owing to the lack of He^+ , the EUV portion of the transmitted spectrum cuts off at a higher energy than found by Dumont et al. (2003).

Overall, our method appears to give reasonably accurate results, with computing times short enough to allow the production of a large grid of reflection models for fitting to observed X-ray spectra.

3 RESULTS

For an optically thick medium, we have calculated model reflection spectra covering a range of values for the ionization parameter ($\xi = 30, 100, 300, 1000, 3000$ and $10\,000 \text{ erg cm s}^{-1}$), the photon index ($\Gamma = 1.0$ to 3.0 in steps of 0.2), and the iron abundance ($A_{Fe} = 0.1, 0.2, 0.5, 1.0, 2.0, 5.0$ and 10.0) relative to its solar value. The result is a grid of 462 reflection models.

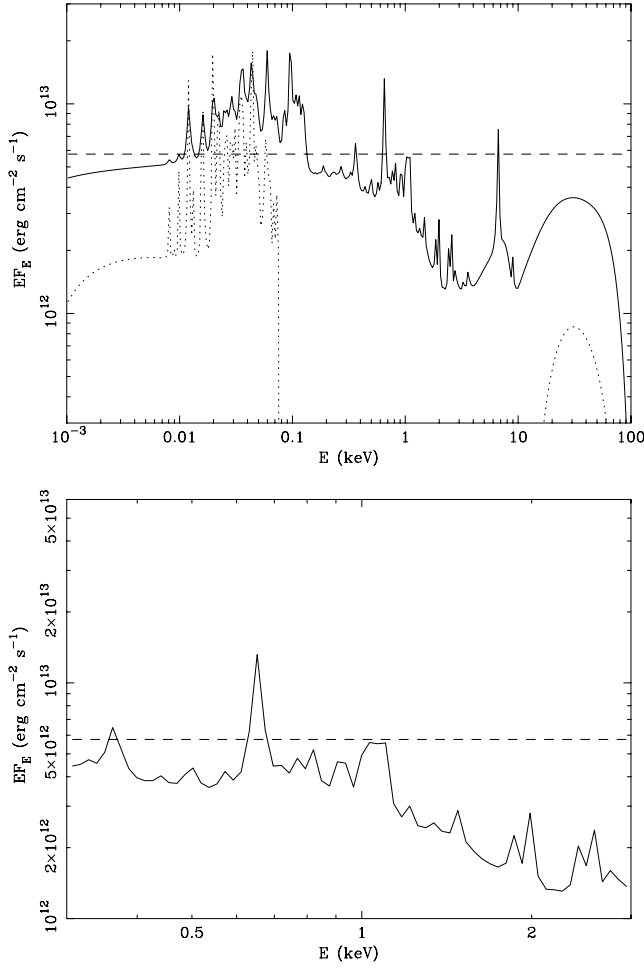


Figure 2. Spectra for the *isolated* slab illuminated on one side. The dashed curve is the illuminating spectrum, the solid curve is the ‘reflected’ spectrum emerging from the illuminated side, and the dotted curve is the ‘transmitted’ spectrum emerging from the far side. The lower panel shows a close-up of a portion of the broader spectrum shown in the upper panel. The spectral resolution is 30.

Of course, the ionization parameter has a marked effect on emission and absorption features in the reflected spectrum. Fig. 3 shows reflected spectra for three different values of ξ . In each case, the incident spectrum has $\Gamma = 2.0$, and iron has solar abundance ($A_{\text{Fe}} = 1$). For $\xi = 10^4$ erg cm s $^{-1}$, the surface layer is highly ionized, with Fe XXV–XXVII dominating for $\tau_T \lesssim 7$. The only important emission feature is the highly Compton-broadened Fe K α line peaking at 7.0 keV. For $\xi = 10^3$ erg cm s $^{-1}$, the illuminated gas is not as highly ionized. Fe XXV dominates for $\tau_T \lesssim 1$, and the lighter elements are no longer fully ionized below that. The strong Fe K α emission is dominated by the Fe XXV intercombination line, and Compton broadening is still important. The spectral region between 0.3 and 3 keV shows K α lines of C VI, O VIII, Ne X, Mg XII, Si XIII–XIV and S XV–XVI, as well as a few Fe L α lines, all atop a shallow absorption trough. The N VII K α line, at an energy (0.50 keV) just above the C VI K edge, is very weak. When ξ is reduced to 10^2 erg cm s $^{-1}$, there is very little ionization for $\tau_T \gtrsim \frac{1}{2}$. The narrow Fe K α line near 6.4 keV is owing to fluorescence, and the spectral region below 3 keV exhibits a myriad of emission features atop a deep absorption trough.

In addition to affecting the overall slope of the reflected spectrum, the photon index Γ also affects the emission and absorption features,

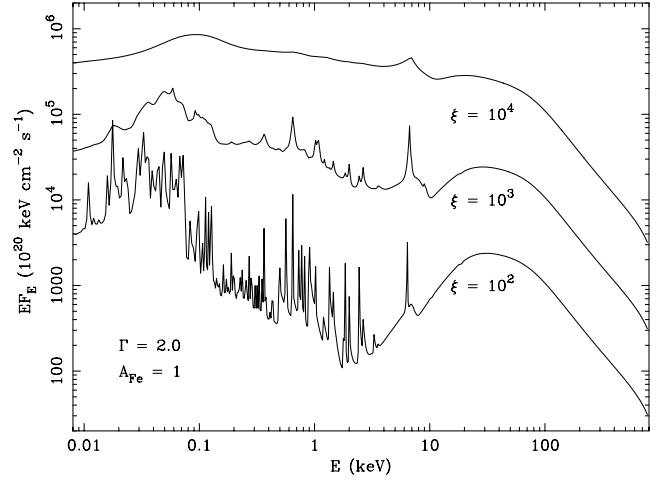


Figure 3. Reflected spectra for three values of the ionization parameter, with $\xi = 10^2$ (bottom curve), 10^3 and 10^4 erg cm s $^{-1}$ (top curve). The incident spectrum has $\Gamma = 2.0$, and iron has solar abundance.

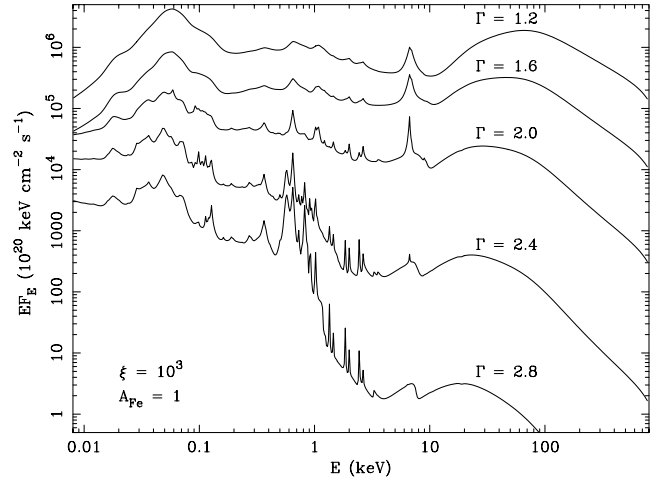


Figure 4. Reflected spectra for five values of the photon index, with $\Gamma = 1.2$ (top curve), 1.6, 2.0, 2.4 and 2.8 (bottom curve). The incident spectrum has $\xi = 10^3$ erg cm s $^{-1}$, and iron has solar abundance. Successive spectra have been offset by factors of 5 for clearer presentation.

as harder illuminating spectra have greater ionizing power. Fig. 4 shows reflected spectra for five different values of Γ . In each case, the incident spectrum has $\xi = 10^3$ erg cm s $^{-1}$, and iron has solar abundance ($A_{\text{Fe}} = 1$). For $\Gamma = 1.2$ or 1.6, the illuminated gas is more highly ionized than for $\Gamma = 2.0$. The Fe K α feature is a broader combination of Fe XXV and Fe XXVI lines, and the lines of the lighter elements are weaker. With $\Gamma = 2.4$ or 2.8, on the other hand, the illuminated gas is less highly ionized. Fe XVIII–XXII dominate at the outer surface instead of Fe XXV, so the Fe K α line is much weaker, while the Fe L α lines are stronger and more numerous. The K α lines of the lighter elements are stronger (as is the continuum absorption), with He-like lines exceeding H-like lines for Mg, Si and S. The oxygen lines are especially enhanced by a soft illuminating spectrum.

The effects of altering the abundance of iron are shown in Fig. 5. Again, the illuminating radiation has $\xi = 10^3$ erg cm s $^{-1}$ and $\Gamma = 2.0$. With iron reduced to 0.2 times its solar abundance, both the K α emission line (6.7 keV) and the K-absorption feature (~ 10 keV)

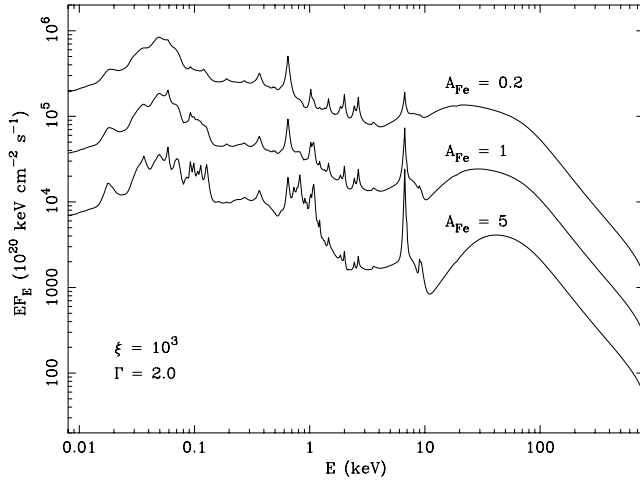


Figure 5. Reflected spectra for three values of the iron abundance, with $A_{\text{Fe}} = 0.2$ (top curve), 1 and 5 (bottom curve) times solar abundance. The incident spectrum has $\xi = 10^3 \text{ erg cm s}^{-1}$ and $\Gamma = 2.0$. Successive spectra have been offset by factors of 5 for clearer presentation.

are reduced compared to the reflected spectrum with solar abundance. Also, less Fe $L\alpha$ emission is blended with the Ne $x K\alpha$ line (1.0 keV). With iron at five times solar abundance, the increased iron absorption lowers the continuum for $1 \lesssim E \lesssim 40 \text{ keV}$, while the Fe $K\alpha$ (6.7 keV), $L\alpha$ ($\sim 1 \text{ keV}$), and $2p \rightarrow 2s$ ($\sim 0.1 \text{ keV}$) emission lines are enhanced. At the same time, the $K\alpha$ lines of Mg, Si and S are weakened, partly because these elements do not remain highly ionized to as great a depth.

The grid of 462 models is being made available as an ionized-reflection model, called REFLION, for use in the XSPEC data-fitting routine (Arnaud 1996).

4 DISCUSSION

The treatment of Ross & Fabian (1993) has been extended to include all commonly important ionization states and transitions. The resulting spectral grids should be useful for interpreting spectra from AGN, BHCs and GRBs. Major signatures of moderately ionized reflection are a Compton hump at about 30 keV, a strong ionized iron line at 6.7 keV, multiple emission lines on top of a soft continuum between 0.3 and 3 keV and a further EUV hump of emission peaking at about 60 eV. The iron abundance has a significant effect on the shape of the reflected continuum between about 3 and 30 keV.

The spectra that we have calculated result entirely from reflection (reprocessed illumination). A significant fraction of the incident X-ray energy emerges as softer radiation (as discussed recently by Madej & Róžańska 2004, for example). The accretion disc beneath the illuminated surface layer can be expected to produce additional soft radiation (the ‘big blue bump’) that can enhance the EUV hump. Fig. 6 shows what happens when the calculations include a soft blackbody spectrum with $kT_{\text{bb}} = 0.010 \text{ keV}$ entering the illuminated layer from below. Models are shown with blackbody fluxes equal to the illuminating flux and ten times greater than the illuminating flux. In both cases, more EUV radiation emerges than for pure reflection, as expected, but the X-ray spectrum is essentially unchanged. Furthermore, accretion power liberated in an accretion disc corona (producing the illumination) should reduce the amount of power liberated locally within the disc, so the ‘big blue bump’ may not be produced in the same regions of the disc as the X-ray

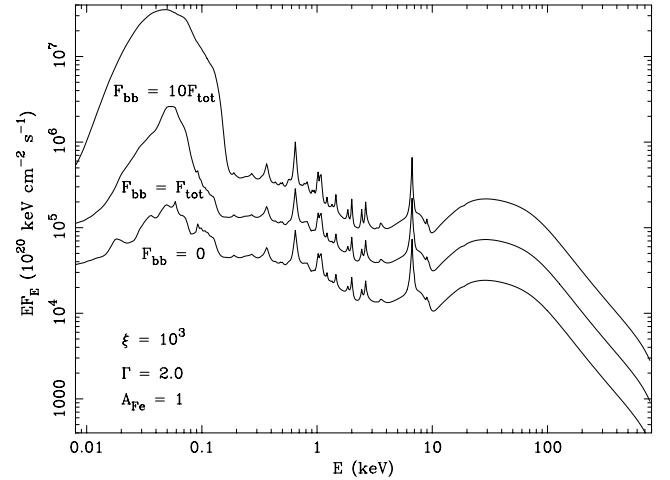


Figure 6. Emergent spectra for pure reflection (bottom curve) and when a soft blackbody spectrum ($kT_{\text{bb}} = 0.010 \text{ keV}$) enters the surface layer from below. Results are shown with the blackbody flux equal to the illuminating flux (middle curve) and ten times greater than the illuminating flux (top curve). The illuminating spectrum has $\xi = 10^3 \text{ erg cm s}^{-1}$ and $\Gamma = 2.0$, and iron has solar abundance. Successive spectra have been offset by factors of 3 for clearer presentation.

reflection. For these reasons, we have chosen to calculate reflection spectra only.

A signature of ionized reflection is the soft excess emission which occurs in the 0.2–2 keV band owing to lines and bremsstrahlung from the hot surface layers. It gives a bump in the relativistically blurred spectrum which, when folded through an *XMM-Newton* pn response matrix in order to simulate real data, is well fitted by a blackbody of temperature 150 eV (residuals less than 10 per cent). This may be relevant to the 100–200 eV temperature component found in the X-ray spectra of many low-redshift PG quasars (Gierlinski & Done 2004; Porquet et al. 2004) which therefore may be owing to ionized reflection.

We have checked whether the many emission features in the reflection spectrum are likely to be readily observable. If there is little to blur the spectrum as a result of either instrumental resolution or shear within the ionized reflector, then the lines will be observable. However, when there is strong shear, as in the inner parts of an accretion disc, then the situation is much more difficult. We show in Fig. 7 the effect of relativistic blurring in an accretion disc inclined at 30° where the emission has an emissivity index of 3 and extends from 3 to 100 gravitational radii. Here $\xi = 10^3 \text{ erg cm s}^{-1}$, $\Gamma = 2.0$ and $A_{\text{Fe}} = 1$. The broad (He-like) Fe K line is very clear, as is a relatively weak broad oxygen line. A weak feature of Fe-L and Ne with about the same equivalent width as O ($\sim 120 \text{ eV}$ relative to the local reflection ‘continuum’ alone), together with Si and S are just discernible in this reflection-only spectrum. Fig. 8 demonstrates how extreme relativistic blurring and changes in iron abundance affect observations of Fe K features. A low iron abundance, perhaps owing to Type II supernovae enrichment, produces a small edge in the spectrum, whereas a high iron abundance, perhaps owing to Type Ia supernovae enrichment, produces an apparent large edge.

ACKNOWLEDGMENTS

RRR and ACF thank the College of the Holy Cross and The Royal Society, respectively, for support.

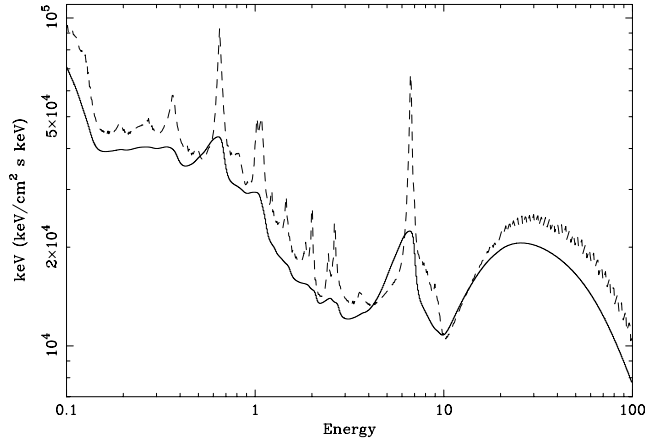


Figure 7. Effect of relativistic blurring on the emergent spectrum. The model with $\xi = 10^3 \text{ erg cm s}^{-1}$, $\Gamma = 2.0$ and $A_{\text{Fe}} = 1$ (central line in Fig. 3, now dashed) has been blurred as if observed from a disc with emissivity index 3 extending from 3 to 100 gravitational radii around a maximal Kerr black hole, viewed at an inclination angle of 30° (solid line).

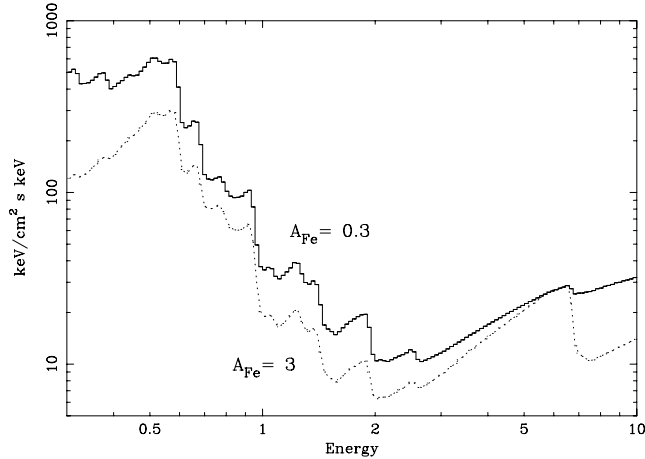


Figure 8. Effects of iron abundance on relativistic-blurred spectra. Models for $\xi = 30 \text{ erg cm s}^{-1}$ and $\Gamma = 2.0$ with $A_{\text{Fe}} = 0.3$ (solid) and $A_{\text{Fe}} = 3$ (dashed) have been blurred as if observed from a disc with emissivity index 3 extending from 2 to 100 gravitational radii around a maximal Kerr black hole, viewed at an inclination angle of 30° .

REFERENCES

- Allen C. W., 1973, *Astrophysical Quantities*. Athlone Press, London
 Arnaud K. A., 1996, in Jacoby G. H., Barnes J., eds, *ASP Conf. Ser. Vol. 101, Astronomical Data Analysis Software and Systems V*. Astron. Soc. Pac., San Francisco, p. 17

- Arnaud M., Raymond J., 1992, *ApJ*, 398, 394
 Arnaud M., Rothenflug R., 1985, *A&AS*, 60, 425
 Ballantyne D. R., Ross R. R., Fabian A. C., 2001, *MNRAS*, 327, 10
 Bates D. R., Dalgarno A., 1962, in Bates D. R., ed., *Atomic and Molecular Processes*. Academic Press, New York, p. 245
 Boller Th. et al., 2002, *MNRAS*, 329, L1
 Burgess A., Summers H. P., 1969, *ApJ*, 157, 1007
 Cooper G., 1971, *Phys. Rev. D*, 3, 2312
 Dere K. P., Landi E., Young P. R., Del Zanna G., 2001, *ApJS*, 134, 331
 Dumont A.-M., Collin S., Paletou F., Coupé S., Godet O., Pelat D., 2003, *A&A*, 407, 13
 Fabian A. C. et al., 2002, *MNRAS*, 335, L1
 Foster A. J., Ross R. R., Fabian A. C., 1986, *MNRAS*, 221, 409
 Gaetz T. J., Salpeter E. E., 1983, *ApJS*, 52, 155
 Gierlinski M., Done C., 2004, *MNRAS*, 349, L7
 Hollenbach D., McKee C. F., 1979, *ApJS*, 41, 555
 Hummer D. G., 1968, *MNRAS*, 138, 73
 Hummer D. G., Rybicki G., 1971, *ARA&A*, 9, 237
 Jacobs V. L., Davis J., Kepple P. C., Blaha M., 1977, *ApJ*, 211, 605
 Kaastra J. S., Mewe R., 1993, *A&AS*, 97, 443
 Kato T., 1976, *ApJS*, 30, 397
 Kompaneets A. S., 1957, *Soviet Phys. JETP*, 4, 730
 Landini M., Monsignori Fossi B. C., 1990, *A&AS*, 82, 229
 Liedahl D. A., Kahn S. M., Osterheld A. L., Goldstein W. H., 1990, *ApJ*, 350, L37
 Madej J., Różańska A., 2004, *MNRAS*, 347, 1266
 Mauche C. W., Liedahl D. A., Mathiesen B. F., Jimenez-Garate M. A., Raymond J. C., 2004, *ApJ*, 606, 168
 Morrison R., McCammon D., 1983, *ApJ*, 270, 119
 Nayakshin S., Kazanas D., Kallman T. R., 2000, *ApJ*, 537, 833
 Nomoto K., Hashimoto M., Tsujimoto T., Thielemann F.-K., Kishimoto N., Kubo Y., Nakasato N., 1997, *Nucl. Phys. A*, 616, 79
 Péquignot D. et al., 2002, in Ferland G. J., Savin D. W., eds, *ASP Conf. Ser. Vol. 247, Spectroscopic Challenges of Photoionized Plasmas*. Astron. Soc. Pac., San Francisco, p. 533
 Porquet D., Reeves J. N., O'Brien P., Brinkmann W., 2004, *A&A*, 422, 85
 Raymond J. C., Smith B. W., 1977, *ApJS*, 35, 419
 Ross R. R., 1979, *ApJ*, 233, 334
 Ross R. R., Fabian A. C., 1993, *MNRAS*, 261, 74
 Ross R. R., Fabian A. C., Brandt W. N., 1996, *MNRAS*, 278, 1082
 Ross R. R., Fabian A. C., Young A. J., 1999, *MNRAS*, 306, 461
 Różańska A., Dumont A.-M., Czerny B., Collin S., 2002, *MNRAS*, 332, 799
 Shemmer O., Netzer H., Maiolino R., Oliva E., Croom S., Corbett E., Di Fabrizio L., 2004, *ApJ*, 614, 547
 Summers H. P., 1974, *Appleton Laboratory, Internal Memo 367*
 Verner D. A., Ferland G. J., 1996, *ApJS*, 103, 467
 Verner D. A., Yakovlev D. G., 1995, *A&AS*, 109, 125
 Verner D. A., Verner E. M., Ferland G. J., 1996, *Atomic Data Nucl. Data Tables*, 64, 1
 Weisheit J. C., 1974, *ApJ*, 190, 735
 Weisheit J. C., Dalgarno A., 1972, *Astrophys. Lett.*, 12, 103
 Życki P. T., Krolik J. H., Zdziarski A. A., Kallman T. R., 1994, *ApJ*, 437, 597

This paper has been typeset from a \LaTeX file prepared by the author.